Nano-Micro Letters

e-ISSN 2150-5551
CN 31-2103/TB

ARTICLE

https://doi.org/10.1007/s40820-024-01337-0

Cite as
Nano-Micro Lett.
(2024) 16:111

Received: 13 September 2023
Accepted: 16 December 2023
Published online: 6 February 2024

Fundamental Understanding of Hydrogen Evolution Reaction on Zinc Anode Surface: A First-Principles Study

Xiaoyu Liu[1], Yiming Guo[1], Fanghua Ning[1] ✉, Yuyu Liu[1], Siqi Shi[2], Qian Li[3], Jiujun Zhang[1], Shigang Lu[1], Jin Yi[1] ✉

HIGHLIGHTS

- The reaction mechanisms of hydrogen evolution reaction (HER) on various crystal surfaces of zinc anode have been systematically investigated by first-principle calculations.
- Both the thermodynamic and kinetic aspects of HER have been studied to reveal the relative HER activity of several crystal surface of zinc anode.
- The generalized coordination number of surface Zn atoms are proposed as a key descriptor of HER activity of Zn anode.

ABSTRACT Hydrogen evolution reaction (HER) has become a key factor affecting the cycling stability of aqueous Zn-ion batteries, while the corresponding fundamental issues involving HER are still unclear. Herein, the reaction mechanisms of HER on various crystalline surfaces have been investigated by first-principle calculations based on density functional theory. It is found that the Volmer step is the rate-limiting step of HER on the Zn (002) and (100) surfaces, while, the reaction rates of HER on the Zn (101), (102) and (103) surfaces are determined by the Tafel step. Moreover, the correlation between HER activity and the generalized coordination number ($\overline{CN}$) of Zn at the surfaces has been revealed. The relatively weaker HER activity on Zn (002) surface can be attributed to the higher $\overline{CN}$ of surface Zn atom. The atomically uneven Zn (002) surface shows significantly higher HER activity than the flat Zn (002) surface as the $\overline{CN}$ of the surface Zn atom is lowered. The $\overline{CN}$ of surface Zn atom is proposed as a key descriptor of HER activity. Tuning the $\overline{CN}$ of surface Zn atom would be a vital strategy to inhibit HER on the Zn anode surface based on the presented theoretical studies. Furthermore, this work provides a theoretical basis for the in-depth understanding of HER on the Zn surface.

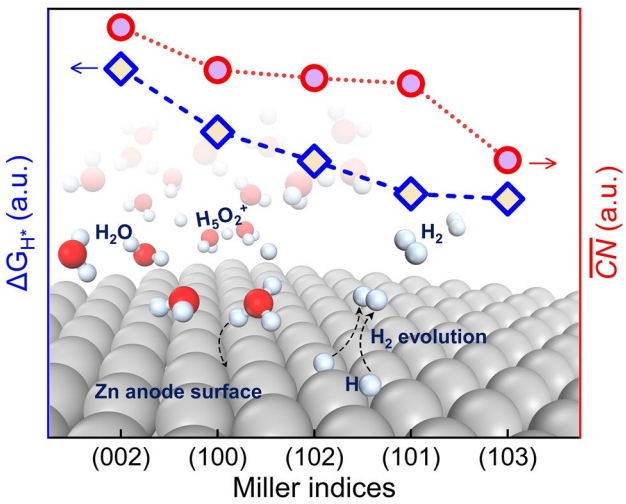

KEYWORDS Aqueous Zn-ion battery; Zn anode; Hydrogen evolution reaction; Coordination number; First-principles calculation

✉ Fanghua Ning, fhning@shu.edu.cn; Jin Yi, jin.yi@shu.edu.cn
[1] Institute for Sustainable Energy & Department of Chemistry, Shanghai University, Shanghai 200444, People's Republic of China
[2] School of Materials Science and Engineering, Shanghai University, Shanghai 200444, People's Republic of China
[3] College of Materials Science and Engineering, National Engineering Research Center for Magnesium Alloys, Chongqing University, Chongqing 400044, People's Republic of China

1 Introduction

The challenges associated with zinc anode, such as dendrite growth, hydrogen evolution reaction (HER), and passivation, have greatly hindered the practical applications of aqueous Zn-ion batteries (AZIBs) [1–5]. The standard electrode potential of Zn^{2+}/Zn (− 0.76 V vs. SHE) in aqueous solution is below the standard electrode potential of HER. The relative potential to initiate Zn^{2+}/Zn deposition and HER depends on both the overpotential of HER and Zn deposition. The hydrogen evolution can lead to swelling of AZIBs, which would result in safety issues [6–9]. In addition, the contact between solid phase and liquid phase will be impeded by the H_2 gas bubbles formed during HER processes, resulting in large polarization potential and even circuit break [10–13]. Meanwhile, the HER will lead to an increase in the pH of the nearby domain [14]. Subsequently, the formation of by-products such as $Zn(OH)_2$, $Zn_4(OH)_6SO_4{\cdot}xH_2O$ will take place due to the increase of pH [15], thus passivating the zinc metal and inhibiting the transport of Zn^{2+} [16–18]. The above-mentioned HER-related side reactions will largely affect the electrochemical performance of AZIBs.

Coating and alloying are common modification strategies for Zn anode to inhibit HER [19–24]. Moreover, tuning the exposed crystal surface of Zn anode has been proposed as an effective strategy. The Zn (002) oriented hexagonal texture parallel to the Zn substrate with high stack density would show less corrosion and dissolution, resulting in improved cycling stability [25–27]. Song et al. have proposed that Zn (002) texture could be obtained via a one-step annealing process on a commercial Zn foil, which has improved the electrochemical performance of Zn anode [28]. In addition, Hao et al. have suggested that the gel electrolyte with sulfonate and imidazole groups could promote Zn deposition with Zn (002) surface exposed, which can suppress HER [29]. The Zn (002) surface has been regarded as the most stable facet against HER [30].

However, the detailed mechanism for the relatively lower HER activity of Zn (002) surface is still unclear. The exposed surface of the primary particles would contain several crystal surfaces, it is difficult to decouple the role of Zn (002) surface via the experimental methods. Fundamentally, the HER activity of a catalyst is determined by the interaction between the intermediates and the catalyst. Sabatier's principle suggests that catalysts with high HER activity must bond with reaction intermediates neither too strongly nor too weakly [31]. The hydrogen adsorption step will be difficult to occur if the hydrogen is too weakly bonded to the surface. The hydrogen liberation step will be limited if the hydrogen is too strongly bonded to the surface [32]. The hydrogen adsorption free energy $\Delta G_{H^*} \sim 0$ based on first-principles calculations are conventionally used as a criterion of the optimal HER activity [33], which is represented in the "volcano" plots [34]. Since only the ΔG_{H^*} with 1/4 monolayer coverage is considered in the conventional "volcano" plot, the effect of hydrogen coverage on ΔG_{H^*} needs to be considered [35]. The *d*-band center is also used to predict the HER activity of transition metals as the ΔG_{H^*} is correlated with the *d*-band center [36]. However, the dependence between the *d*-band center and HER activity is untenable in some cases. For example, the *d* band center of Ni and Pt are almost the same, while Ni is more inert than Pt in terms of HER. Focusing on the HER activity of the Zn anode, the fully filled *d* bands of Zn make it more difficult to elucidate the relative HER activity of different facets of Zn metal from electronic structures. Therefore, a more specific descriptor to evaluate HER activity at different Zn surfaces and a fundamental understanding of the HER activity are needed, which would yield more specific strategies to inhibit HER at the Zn anode surface.

In this work, the HER activities on several crystal surfaces containing the Zn (002), (100), (101), (102), and (103) surfaces are explored from both the thermodynamic and kinetic aspects via first-principles calculations. The hydrogen adsorption free energy (ΔG_{H^*}) and the activation barrier of Volmer and Tafel steps at the above Zn surfaces have been calculated. The mechanisms of the relatively weaker HER activity on the Zn (002) surface are revealed, which can be attributed to the higher $\overline{CN}$ of surface Zn atom. Once the surface of the Zn (002) slab mode is not flat at an atomic level, the uneven Zn (002) surface would show significantly higher HER activity than the flat Zn (002) surface. The $\overline{CN}$ of the surface Zn atom is proposed as a key descriptor of HER activity. According to the key descriptor of $\overline{CN}$, the most stable adsorption site for the H atom and the HER activity could be predicted. Tuning the $\overline{CN}$ of surface Zn atom would be a vital strategy to inhibit HER on the Zn anode.

https://doi.org/10.1007/s40820-024-01337-0

2 Computational Details

First-principles calculations based on density-functional theory (DFT) in this work were performed in the Vienna ab-initio simulation package (VASP) [37]. The Perdew Burke-Ernzerhof (PBE) [38] pseudopotentials and projector-enhanced wave (PAW) [39] were used. The cutoff energy for the plane-wave basis set was set to 520 eV. The k-points settings are listed in Table S1. Gamma centered grid was applied for Brillouin zone integration. The Zn crystal surfaces were constructed by using the slab model with a symmetric slab containing a vacuum layer (> 15 Å), which can avoid interactions between adjacent slabs. The detailed information of slab models is provided in Table S1 and Fig. S1. The convergence threshold was set as 10^{-5} eV in energy and 0.01 eV/Å in force. The transition state of HER was calculated using the CI-NEB [40] and dimer [41] methods.

The surface energy (γ) was calculated based on Eq. (1):

$$\gamma = \frac{E_{slab} - E_{bulk} \times n_{slab}}{2 \times A_{slab}} \quad (1)$$

where E_{slab} is the total energy of the slab model, E_{bulk} is the average energy per Zn atom in the bulk model of Zn metal, n is the number of Zn atoms in the slab model, and A_{slab} is the surface area.

The hydrogen adsorption energies (ΔE_{H^*}) is defined as Eq. (2):

$$\Delta E_{H^*} = \frac{E_{nH^*} - E_{Zn} - \frac{n}{2}E_{H_2}}{n} \quad (2)$$

where E_{nH^*} is the total energy of the slab with n H atoms adsorbed, E_{Zn} is the energy of the Zn slab model, and E_{H_2} is the energy of the H_2 molecule in the gas phase state.

The hydrogen adsorption free energies (ΔG_{H^*}) were calculated based on Eq. (3):

$$\begin{aligned}\Delta G_{H^*} &= \Delta E_{H^*} + \Delta ZPE - T\Delta S \\ &= \Delta E_{H^*} + ZPE_{H^*} - \frac{1}{2}\mathrm{ZPE}_{H_2} - TS_{H^*} + \frac{1}{2}TS_{H_2}\end{aligned} \quad (3)$$

where the ΔE_{H^*} is defined in Eq. (2). The temperature is set to 300 K. The ZPE_{H^*}, S_{H^*}, ZPE_{H_2}, and S_{H_2} are the zero-point vibration energy and entropy of H that adsorbed on Zn surface and gas phase H_2 under standard atmospheric pressure, respectively.

The generalized coordination number ($\overline{CN}$) of the surface Zn atom is defined as Eq. (4):

$$\overline{CN}(i) = \sum_{j=1}^{n_i} \frac{cn(j)}{cn_{max}} \quad (4)$$

where $cn(j)$ is the coordination number of zinc atoms adjacent to zinc and cn_{max} is the maximum atomic coordination number of Zn atom in Zn metal [42].

3 Results and Discussion

3.1 Hydrogen Adsorption at Zn Surfaces

The HER activity on different surfaces of the Zn anode is determined by the intrinsic properties of Zn surface. It is necessary to investigate the properties of different Zn surfaces. Zn metal presents a typical hexagonal close-packed (hcp) structure. The optimized structures of Zn (002), (100), (101), (102), and (103) surfaces are shown in the inserts of Fig. 1a. The Zn (002) surface shows the close-packed arrangement within the surface. Other surfaces yielded structural rearrangement to some extent during the structural optimization processes. Especially, the uneven Zn (100) surface becomes flat surface at an atomic level after optimization. Consequently, the optimized Zn (002) and (100) surfaces are flat at an atomic level, while the optimized Zn

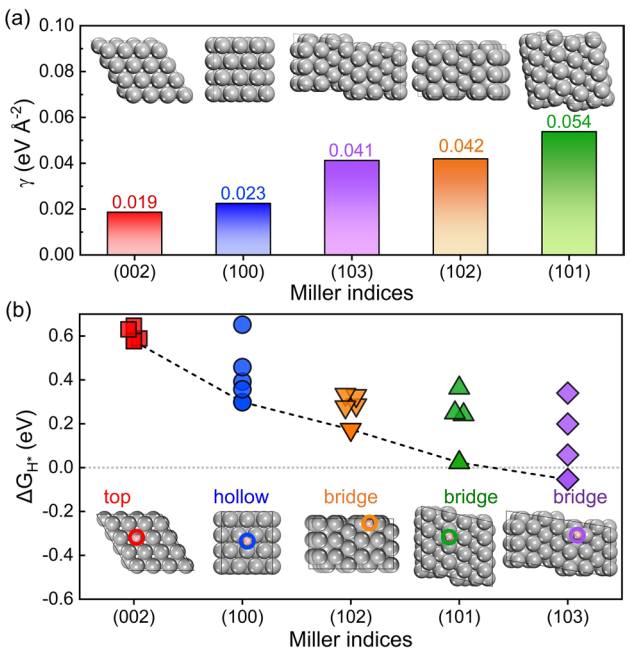

Fig. 1 **a** The surface energies of the crystal surfaces of Zn metal with different Miller indices. **b** The ΔG_{H^*} for H atom adsorbed at different sites of the crystal surfaces of zinc metal

(101), (102), and (103) surfaces are uneven at an atomic level.

The surface energies of the above crystal surfaces are calculated, as shown in Fig. 1a. In general, the surface energies are agreement with the database provided in the materials project [43], implying that the structural optimization of the above crystal surfaces of Zn metal is rational. It can be seen that the surface energy of the (002) surface is the lowest, indicating that (002) is more stable than other surfaces. The surface energy of the (100) surface is much lower when compared to that of the (101), (102), and (103) surfaces. Atomically flat surfaces are more stable than uneven surfaces. The crystal surfaces with higher surface energy are expected to present higher reaction activity for oxidation or corrosion [44]. In contrast, the crystal surfaces with lower surface energy are expected to show better stability against interface reactions.

The hydrogen-adsorption free energy (ΔG_{H^*}) is used to predict the HER activity of catalysts from a thermodynamic aspect. According to Sabatier's principle [31], a good HER activity of catalysts need to bond with the H atom neither too strongly nor too weakly. If the H atom bonded to the surface too weakly, the H adsorption step (Volmer) will be difficult to take place. In contrast, the desorption (Heyrovsky/Tafel) step will hard to be proceed when H bonded to the surface too strongly [32]. $\Delta G_{H^*} \sim 0$ is regarded as the optimal value for good HER activity from the thermodynamic point of view [45]. Thus, ΔG_{H^*} at different site of Zn (002), (100), (101), (102), and (103) surfaces were calculated to insight into the thermodynamic aspect of HER activity of Zn anode, as shown in Fig. 1b. In addition, Van der Waals interactions with Grimme's D3 scheme have been tested for hydrogen-adsorption models (Fig. S2). The ΔG_{H^*} values are slightly changed, while the relative values of ΔG_{H^*} for several crystal surfaces are almost unchanged after considering the Van der Waals interactions. The most stable adsorption site for each crystal surface is identified, which is presented in the insert of Fig. 1b. The adsorption energies of H atoms at bridge sites on the (101), (102), and (103) surfaces are significantly lower than those at other sites, suggesting that the bridge sites are the most stable adsorption site for (101), (102), and (103) surfaces. The detailed ΔG_{H^*} values and the corresponding structures of H adsorbed at (101), (102), and (103) surfaces are shown in Tables S2–S4 in the supporting information, respectively. And H prefers to be absorbed on the top and hollow sites of (002) and (100) surfaces, respectively. All the adsorption sites and the correspongding ΔG_{H^*} values at (002) and (100) surfaces that were considered here are shown in Tables S5, S6 in the supporting information, respectively. However, the bridge site adsorption becomes more stable as the H coverage increases, which will be discussed in the following part. The lowest value of ΔG_{H^*} for the Zn (002) surface is the highest one among several crystal surfaces. The Zn (002) and (100) surfaces show higher ΔG_{H^*} for the most stable adsorption site than (101), (102), and (103) surfaces. Keep in mind that the above values of ΔG_{H^*} are calculated at a low hydrogen coverage, and the hydrogen coverages are not the same for different crystal surfaces of Zn metal. Besides, H_2O adsorption energies on several crystal surfaces have been calculated (Fig. S3). The adsorption energy differences are within 0.1 eV. Generally, the trends of H_2O adsorption energies are similar to the H adsorption energies. The (002) surface shows the highest H_2O adsorption energy, indicating that H_2O molecules are less likely to adsorbed at (002) surface.

Considering that the hydrogen coverage presents a significant impact on the hydrogen-adsorption energy on other catalyst surfaces like Pt (111) surface [46, 47], the ΔG_{H^*} and ΔE_{H^*} as a function of hydrogen coverage was further investigated, as shown in Figs. 2 and S4, respectively. The details for thermal corrections to Gibbs free energies are listed in Tables S7, S8. The most stable adsorption sites (i.e. the bridge sites) of (101), (102), and (103) surfaces are included. Both the bridge and top sites of (002) crystal face have been conducted because of the small difference of ΔG_{H^*} between the two sites at a low hydrogen coverage. Similarly, both the bridge and hollow sites of (100) crystal

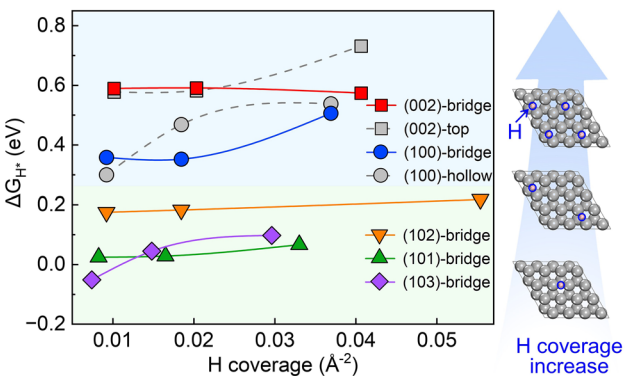

Fig. 2 Hydrogen adsorption energy (ΔG_{H^*}) at several crystal surfaces of the zinc anode as a function of different hydrogen coverage. The H coverage indicates the number of hydrogens absorbed per unit area

https://doi.org/10.1007/s40820-024-01337-0

face have been included due to the small difference of ΔG_{H^*}. The H adsorption energies increase as coverage increases. The relative values of adsorption energy between Zn (002), (100), (101), and (102) surfaces at a certain hydrogen coverage are similar. As for the Zn (103) surface, the adsorption energy increases more significantly than the other surfaces. The Zn (103) surface shows the lowest ΔE_H at low hydrogen coverage, however, the ΔE_H of the (103) surface becomes higher than that of the (101) surface as the hydrogen coverage increases. The Zn (002) surface presents the highest adsorption energy, and Zn (100) surface takes the second place. The Zn (101), (102), and (103) surfaces show relatively lower adsorption energies than Zn (002) and (100) surfaces. We found that the most remarkable difference between the former surfaces (the Zn (101), (102), and (103) surfaces) and the later surfaces (the Zn (002) and (100) surface) is whether the surface is flat at an atomic level. The flat surfaces tended towards higher adsorption energies, which will be discussed quantitatively later. The Zn (002) surface is expected to be the most stable surface against HER from the thermodynamic point of view. Thus, the relative hydrogen adsorption energies for different crystal surfaces of Zn anode at various hydrogen coverages are clarified, which provides a systematic thermodynamic understanding of the HER activity on each crystal surface of Zn anode.

3.2 HER Kinetic Steps at Zn Surfaces

The HER activity cannot be determined just by the thermodynamic perspective. The challenge to the $\Delta G_{H^*} \sim 0$ explanation of HER has been proposed by Peterson and co-workers [45]. The dynamic aspects of HER were further studied. HER is a classical two-electron-transfer reaction that can be carried out by either the Volmer–Heyrovsky or the Volmer–Tafel mechanism [48].

In an acidic solution, proton and electron are transferred to the surface via the Volmer step is defined as Eq. (5) [49]:

$$H^+ + e^- + * \rightarrow H^* \text{ (Volmer)} \quad (5)$$

In order to simulate the Volmer reaction, the Zundel-type hydrated proton ($H_5O_2^+$) [50] is used as the proton donor. The $H_5O_2^+$ lay parallelly at the Zn (002) and (100) surfaces with a distance of about 3 Å. And the $H_5O_2^+$ is oblique to the (101), (102) and (103) surfaces. Figure 3 illustrates the reaction pathway of the Volmer step. The protons are adsorbed at the site with the lowest adsorption energy on the Zn surface after being released from $H_5O_2^+$. Meantime, the two H_2O molecules move to the solution. This is an exothermic process (Fig. 3). An activation barrier up to 1.231 eV is delivered between the initial and transition states for the Volmer step on the (002) surface. The (100) surface also shows a relatively high activation barrier of 0.935 eV. The activation energy barriers of the (101), (102), and (103) surfaces are closer to each other, which are significantly lower than those of the (002) and (100) surfaces. The electrostatic potentials of several crystal surface model are visualized in Fig. S5. The more positive values of electrostatic potential for (101), (102), and (103) surfaces indicate that these surfaces are favorable for electron transfer. Thus, the Volmer step would be easier for (101), (102), and (103) surfaces. The Volmer step at Zn (002) surface would be the most difficult to proceed. Furthermore, the variation trends of the energy barrier values of the Volmer step and the hydrogen adsorption energy ΔG_{H^*} on different crystal surfaces in Fig. 2 are similar. It further proves the correlation between the adsorption energy ΔG_{H^*} and the kinetic of the Volmer reaction.

The surface-bound hydrogen formed in the Volmer step would undergo a H_2 liberation step. The Tafel steps ($2H^* \rightarrow H_2$) show lower energy barriers than Heyrovsky steps ($H^* + H^+ + e^- \rightarrow H_2$) (Fig. S6), thus we focused on Tafel reaction steps. The desorption of two nearby H atoms forms a H_2 molecule with a bond length of ~ 0.75 Å and a distance of > 3.5 Å from the surface. The similar adsorption energies of H_2 at different surface range from − 0.02 to 0.01 eV, which is approximately 0 eV, indicating weak physical adsorption between the H_2 molecule and the surfaces. Figure 4 shows the reaction pathways and the activation barriers of the Tafel reactions at different Zn surfaces. The Zn (101), (102), and (103) surfaces that are uneven at an atomic level show similar energy barriers, which is higher than the Zn (002) and (100) surfaces, indicating that the reaction rate of Tafel step would be slower for Zn (101), (102), and (103) surfaces.

Combining the activation barriers of the Volmer and Tafel steps, it is found that the Volmer step is the rate-limiting step of HER for the Zn (002) and (100) surfaces, while the Tafel step turned to the rate-limiting step for Zn (101), (102), and (103) surfaces. The overall reaction barrier of HER at the Zn (002) surface is significantly higher than that of HER at the Zn (100), (101), (102), and (103) surfaces. The Zn (002) surface is expected to be the most stable surface against

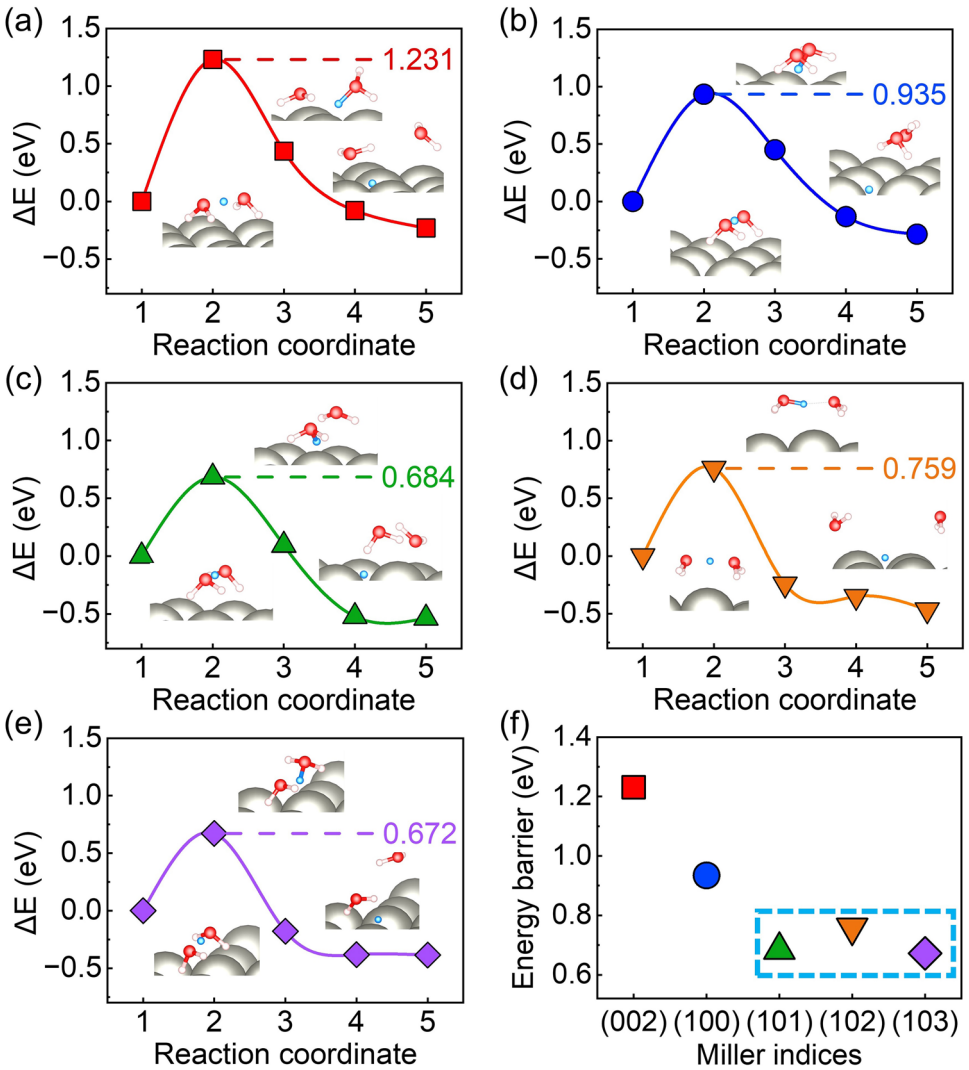

Fig. 3 The energy barriers and reaction pathways of Volmer step on several crystal surface of Zn anode. **a** Zn (002) surface, **b** Zn (100) surface, **c** Zn (101) surface, **d** Zn (102) surface, **e** Zn (103) surface, **f** the comparative Volmer reaction barriers. The insets are the structures of corresponding initial, transition, and final states. The white, red, and grey spheres are H, O, and Zn atoms, respectively. The blue spheres are the protons that are willing to adsorb at the surfaces

HER from both the thermodynamic and dynamic point of view, which is consistent with previous experimental results [51–53].

3.3 Relationship Between $\overline{CN}$ and HER Activity

As is mentioned above, the most remarkable difference between the former surfaces (the Zn (101), (102), and (103) surfaces) and the later surfaces (the Zn (002) and (100) surface) is whether the surface is flat at an atomic level. Considering the similar hydrogen adsorption energies and activation barriers of HER at Zn (101), (102), and (103) surface, the mechanisms of the difference between the atomically flat surfaces and uneven surfaces are further analyzed. The quantitative descriptor for the qualitative features of the atomically flat and uneven surfaces should be identified.

The Zn atoms at the surface show unsaturated coordination, and thus exhibit the activity to adsorb atoms, ions, and molecules. The upper Zn atoms at the atomically uneven surfaces would present a lower nearest neighbor coordination number (*CN*) than the Zn atoms at the atomically flat surfaces. Indeed, as mentioned above in Fig. 1b and Tables S2–S6 in the supporting information, the upper

 https://doi.org/10.1007/s40820-024-01337-0

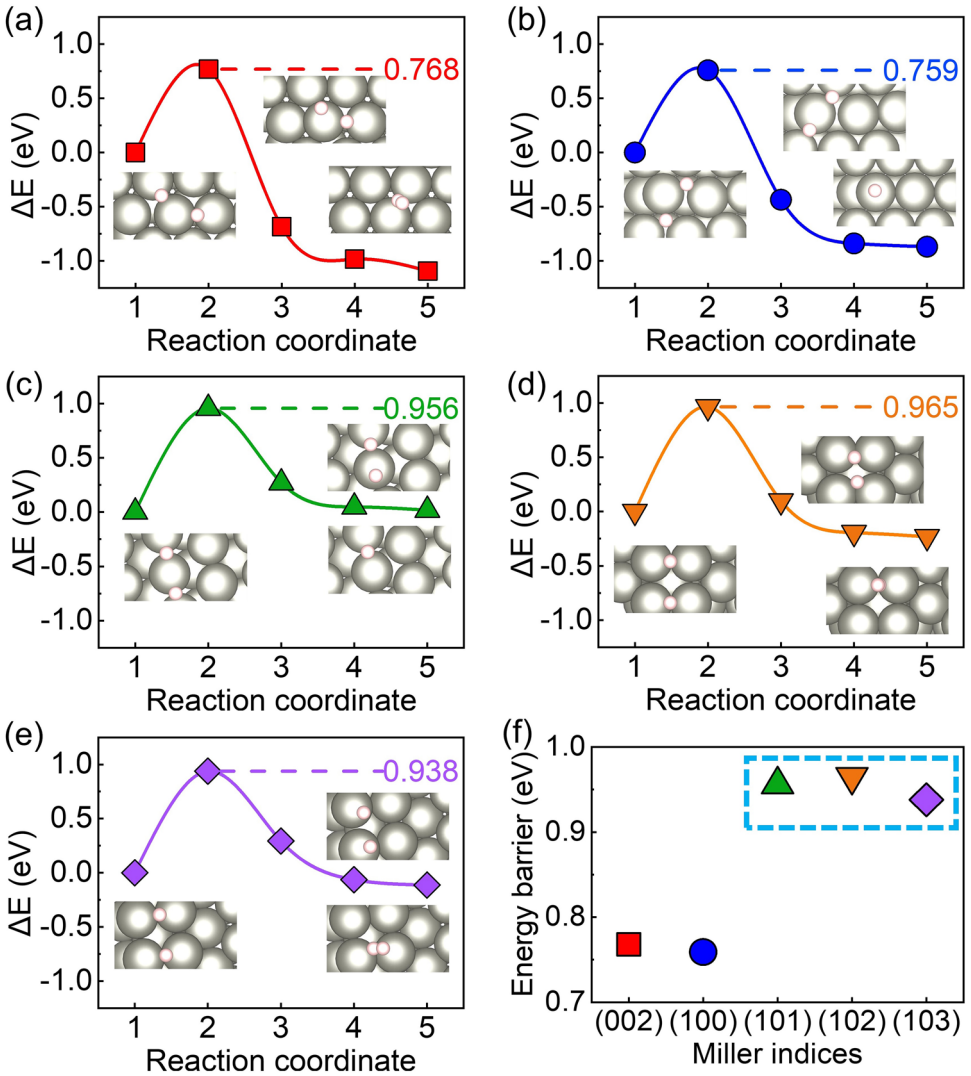

Fig. 4 The energy barriers and reaction pathways of Tafel step on several crystal surface of Zn anode. **a** Zn (002) surface, **b** Zn (100) surface, **c** Zn (101) surface, **d** Zn (102) surface, **e** Zn (103) surface, **f** the comparative Tafel reaction barriers. The insets are the structures of corresponding initial, transition, and final states. The white and grey spheres are H and Zn atoms, respectively

Zn atoms of uneven (101), (102), and (103) surfaces show lower hydrogen adsorption energies, which is the most stable adsorption site and the active site for HER. The *CN* of the surface Zn atom is expected as a quantitative descriptor of the difference between the atomically flat and uneven surface. However, *CN* for the Zn atom at the (100), (101), and (102) surfaces are the same, which cannot interpret the relative H adsorption energies. Extended from conventional *CN*, the generalized coordination number ($\overline{CN}$) proposed by Calle-Vallejo [42] and co-workers could identify the atomic arrangement of the surface atoms more precisely by considering the coordination number of their nearest neighbors. The $\overline{CN}$ has been proposed to make a fast prediction of adsorption properties for platinum nanoparticles. Thus, the $\overline{CN}$ was considered as the quantitative descriptor of the difference between the atomically flat and uneven surface.

The $\overline{CN}$ of Zn atom at the site with the lowest hydrogen adsorption energy was calculated, as shown in Fig. 5. The atomically flat (002) surface shows the largest $\overline{CN}$, and the atomically flat (100) surface takes the second place. The (101), (102), and (103) show relatively lower $\overline{CN}$. As shown in Fig. 5f, there is a correlation between $\overline{CN}$ and the lowest

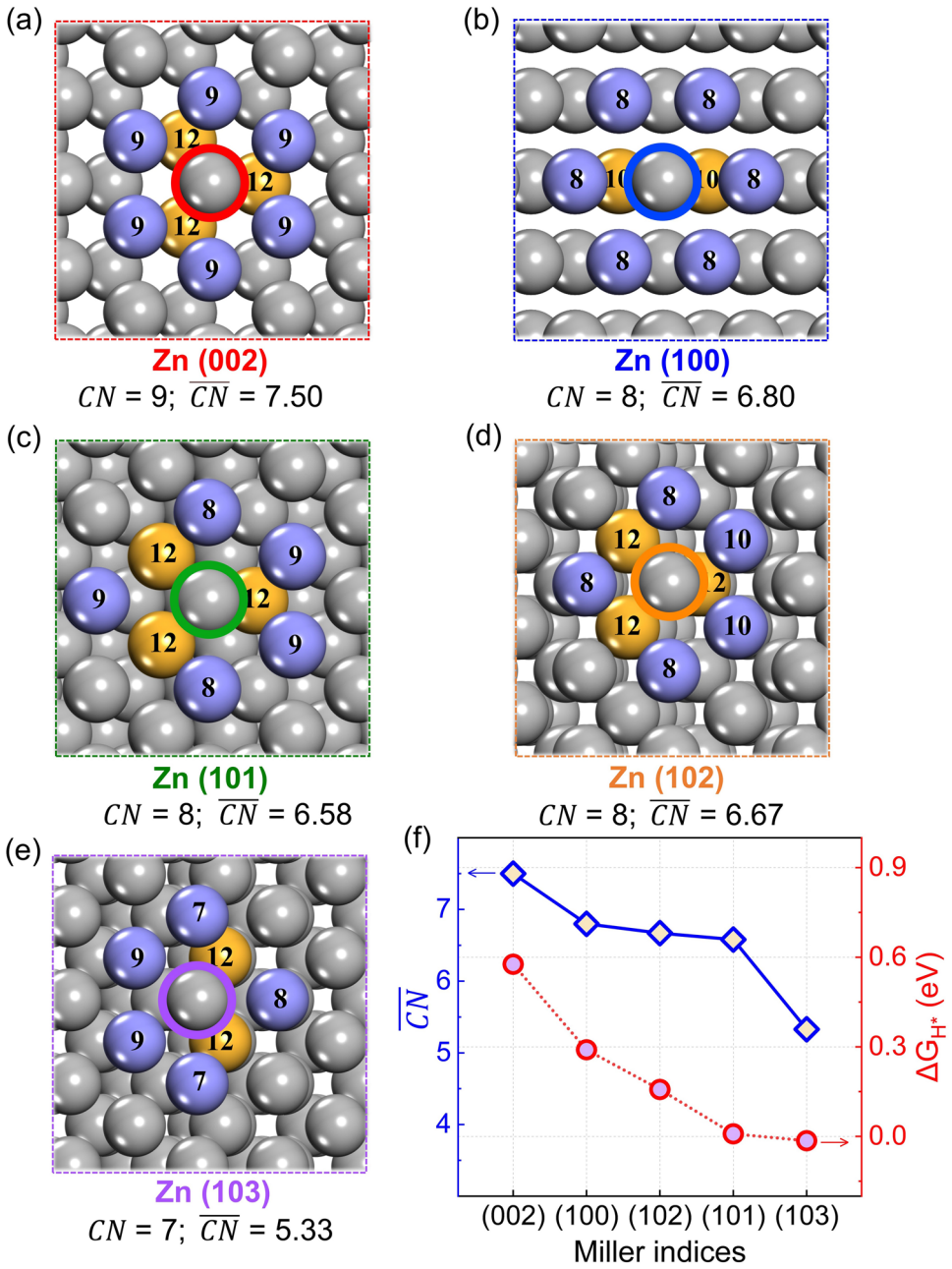

Fig. 5 The schematic diagram of the $\overline{CN}$ of Zn atom at several crystal surface of Zn anode. **a** Zn (002) surface, **b** Zn (100) surface, **c** Zn (101) surface, **d** Zn (102) surface, **e** Zn (103) surface, **f** the correlation between the hydrogen adsorption energy and the $\overline{CN}$

adsorption energy of each surface. The adsorption energy increases with the increase of $\overline{CN}$, which also suggests that the concept of $\overline{CN}$ is also applicable among transition metal Zn. It is also worth noting that H atoms tend to be adsorbed near the Zn with low $\overline{CN}$. A higher $\overline{CN}$ of Zn atoms on crystal surface of Zn anode would deliver higher ΔG_{H^*}, which lead to poor HER activity. Zinc atom in the bulk of zinc metal crystal follows a face centered cubic arrangement, whose $\overline{CN}$ is 12. The $\overline{CN}$ of Zn atom at crystal surface with unsaturated coordination is lower than 12, which tends to form new bonds to compensate for the absence of coordination atoms. Thus, lower $\overline{CN}$ would lead to relatively stronger interaction between H and Zn atoms, indicating lower hydrogen adsorption energy and higher HER activity.

https://doi.org/10.1007/s40820-024-01337-0

The relationship between generalized coordination number ($\overline{CN}$) and HER activity of Zn anode have been revealed. The different $\overline{CN}$ of surface Zn atoms would lead to differences in charge distribution. The correlation between the Bader charge and $\overline{CN}$ have been provided (Fig. S7 and Table S9). The Bader charge decreases as the $\overline{CN}$ increases. Besides, the differential charge density induced by H adsorption for several crystal surfaces are shown in Fig. S8. The differences of Bader charge and differential charge density for several crystal surfaces are very small, which might be caused by the completely filled *d*-bands of Zn atom. Thus, it is hard to explain the HER activity by the charge density.

In order to further verify the correlation between $\overline{CN}$ and adsorption energy, the $\overline{CN}$ and adsorption energies for different adsorption sites of the same crystal surfaces have been further studied. As for uneven surface, including (101), (102), and (103) surfaces, the $\overline{CN}$ of Zn atoms vary within the same crystal surface. The ΔG_{H^*} for adsorption sites with higher $\overline{CN}$ are higher (Figs. 6b and S9), which is consist with the relationship between $\overline{CN}$ and ΔG_{H^*}. The (002) and (100) surfaces are flat at an atomic level, within which the $\overline{CN}$ of each Zn atoms at the same surface are the same, which are 7.50 and 6.80, respectively. Thus, a row of zinc atoms has been added on the atomically flat (002) and (100) crystal surfaces to tune the $\overline{CN}$ of surface Zn atoms, yielding uneven (002) and (100) surfaces, as shown in Fig. 6a. The $\overline{CN}$ of the upper Zn atoms at the uneven (002) surface dropped dramatically from 7.50 to 3.82. As shown in Figs. 6b, S10, and S11, the H adsorption energies of uneven Zn (002) surface are significantly lowered as compared to the original flat (002) surface, regardless of the top site or bridge site, confirming the correlation between $\overline{CN}$ and adsorption energy. The lowest adsorption energies even approximate to 0 eV. Therefore, it is the higher $\overline{CN}$ of atomically flat Zn (002) surface that delivers inert HER activity. Once the Zn (002) surface is uneven at an atomic level, the HER activity is no longer inert. Similarly, the upper Zn atoms at the reconstructed uneven (100) surface with lowered $\overline{CN}$ show lower ΔG_{H^*} (Figs. 6b and S10), which further confirming the relationship between $\overline{CN}$ and ΔG_{H^*}. As a result, the $\overline{CN}$ of the surface Zn atom is proposed as a key descriptor of HER activity.

The surface Zn atoms with higher generalized coordination numbers would show lower HER activity. Zn (002) plane is more conducive to suppressing HER, and lots of efforts have already been made to achieve Zn anode with (002) crystal plane preferred exposed surface. On the other hand, considering that the edge sites would hold lower generalized coordination numbers, edge site should be minimized via increasing the particle size or additive design.

4 Conclusions

In summary, HER activities on several crystal surfaces containing Zn (002), (100), (101), (102), and (103) surfaces are studied from both the thermodynamic and kinetic aspects in this work. The obtained results show that the adsorption free energy (ΔG_H) of a hydrogen atom adsorbed on Zn (002) and (100) surfaces are higher than that on Zn (101), (102), and (103) surfaces. The rate-limiting step

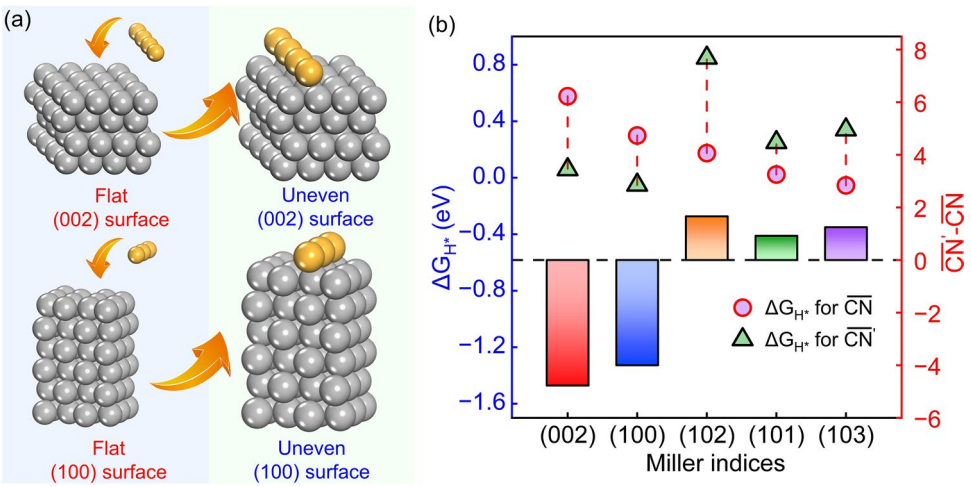

Fig. 6 **a** Schematic diagram of uneven (002) and (100) surface. **b** Hydrogen adsorption energy of H adsorbed on surface Zn atom with different $\overline{CN}$

of HER on the Zn (002) and (100) surfaces is the Volmer step, whereas the HER activity on the Zn (101), (102), and (103) surfaces is restricted by the Tafel step. The Zn (002) and (100) surfaces are flat at an atomic level in the used structural model, while the Zn (101), (102), and (103) surfaces are uneven surface at an atomic level. The atomically flat (002) and (100) surfaces would process higher generalized coordination numbers than uneven (101), (102), and (103) surfaces. The Zn atoms at a flat surface would process a higher coordination number. The mechanisms of the relatively weaker HER activity on the Zn (002) surface are revealed, which can be attributed to the higher $\overline{CN}$ of surface Zn atom. Once the surface of Zn (002) or Zn (100) slab modes is not flat at an atomic level, the uneven Zn (002) surface and Zn (100) surface would show significantly higher HER activity than the flat Zn (002) surface. The $\overline{CN}$ of the surface Zn atom is proposed as a key descriptor of HER activity after our comprehensive analysis. According to the key descriptor $\overline{CN}$, the most stable adsorption site for the H atom and the HER activity could be predicted. It is proposed that tuning the $\overline{CN}$ of the surface Zn atom would be a vital strategy to inhibit HER on the Zn anode. From a visualized perspective, the exposed surface of Zn anode needs to be flat at an atomic level to avoid HER at the surface. This work provides a theoretical understanding of HER on the Zn surface and a guideline to suppress HER on the Zn anode.

Acknowledgements This work was financially supported by the National Natural Science Foundation of China (22075171), Natural Science Foundation of Shanghai (23ZR1423400). The first-principles calculations were supported by the High Performance Computing Center of Shanghai University.

Declarations

Conflict of Interest The authors declare no interest confict. They have no known competing financial interests or personal relationships that could have appeared to influence the work reported in this paper.

Supplementary Information The online version contains supplementary material available at https://doi.org/10.1007/s40820-024-01337-0.

References

1. Z. Li, A.W. Robertson, Electrolyte engineering strategies for regulation of the Zn metal anode in aqueous Zn-ion batteries. Battery Energy **2**(1), 20220029 (2023). https://doi.org/10.1002/bte2.20220029
2. C. Nie, G. Wang, D. Wang, M. Wang, X. Gao et al., Recent progress on Zn anodes for advanced aqueous zinc-ion batteries. Adv. Energy Mater. **13**(28), 2300606 (2023). https://doi.org/10.1002/aenm.202300606
3. B. Li, X. Zhang, T. Wang, Z. He, B. Lu et al., Interfacial engineering strategy for high-performance Zn metal anodes. Nano-Micro Lett. **14**, 6 (2021). https://doi.org/10.1007/s40820-021-00764-7
4. Q. Wen, H. Fu, R.-D. Cui, H.-Z. Chen, R.-H. Ji et al., Recent advances in interfacial modification of zinc anode for aqueous rechargeable zinc ion batteries. J. Energy Chem. **83**, 287–303 (2023). https://doi.org/10.1016/j.jechem.2023.03.059
5. N.S. Alghamdi, M. Rana, X. Peng, Y. Huang, J. Lee et al., Zinc–bromine rechargeable batteries: From device configuration, electrochemistry, material to performance evaluation. Nano-Micro Lett. **15**, 209 (2023). https://doi.org/10.1007/s40820-023-01174-7
6. J.Y. Kim, G. Liu, R.E.A. Ardhi, J. Park, H. Kim et al., Stable Zn metal anodes with limited Zn-doping in MgF_2 interphase for fast and uniformly ionic flux. Nano-Micro Lett. **14**, 46 (2022). https://doi.org/10.1007/s40820-021-00788-z
7. Y. Liu, Y. Liu, X. Wu, Toward long-life aqueous zinc ion batteries by constructing stable zinc anodes. Chem. Rec. **22**, e202200088 (2022). https://doi.org/10.1002/tcr.202200088
8. H. Yu, D. Chen, T. Zhang, M. Fu, J. Cai et al., Insight on the double-edged sword role of water molecules in the anode of aqueous zinc-ion batteries. Small Struct. **3**(12), 2200143 (2022). https://doi.org/10.1002/sstr.202200143
9. D. Yao, D. Yu, S. Yao, Z. Lu, G. Li et al., Interfacial engineering boosts highly reversible zinc metal for aqueous zinc-ion batteries. ACS Appl. Mater. Interfaces **15**(13), 16584–16592 (2023). https://doi.org/10.1021/acsami.2c20075
10. L. Wang, W. Huang, W. Guo, Z.H. Guo, C. Chang et al., Sn alloying to inhibit hydrogen evolution of Zn metal anode in rechargeable aqueous batteries. Adv. Funct. Mater. **32**(1), 2108533 (2022). https://doi.org/10.1002/adfm.202108533
11. J. Chen, W. Zhao, J. Jiang, X. Zhao, S. Zheng et al., Challenges and perspectives of hydrogen evolution-free aqueous Zn-ion batteries. Energy Storage Mater. **59**, 102767 (2023). https://doi.org/10.1016/j.ensm.2023.04.006

12. C.-C. Kao, C. Ye, J. Hao, J. Shan, H. Li et al., Suppressing hydrogen evolution via anticatalytic interfaces toward highly efficient aqueous Zn-ion batteries. ACS Nano **17**(4), 3948–3957 (2023). https://doi.org/10.1021/acsnano.2c12587
13. A. Bayaguud, Y. Fu, C. Zhu, Interfacial parasitic reactions of zinc anodes in zinc ion batteries: Underestimated corrosion and hydrogen evolution reactions and their suppression strategies. J. Energy Chem. **64**, 246–262 (2022). https://doi.org/10.1016/j.jechem.2021.04.016
14. Q. Yang, L. Li, T. Hussain, D. Wang, L. Hui et al., Stabilizing interface pH by N-modified graphdiyne for dendrite-free and high-rate aqueous Zn-ion batteries. Angew. Chem. Int. Ed. **61**(6), e202112304 (2022). https://doi.org/10.1002/anie.202112304
15. Y. Gong, B. Wang, H. Ren, D. Li, D. Wang et al., Recent advances in structural optimization and surface modification on current collectors for high-performance zinc anode: Principles, strategies, and challenges. Nano-Micro Lett. **15**, 208 (2023). https://doi.org/10.1007/s40820-023-01177-4
16. J. Hao, L. Yuan, Y. Zhu, M. Jaroniec, S.-Z. Qiao, Triple-function electrolyte regulation toward advanced aqueous Zn-ion batteries. Adv. Mater. **34**(44), e2206963 (2022). https://doi.org/10.1002/adma.202206963
17. J. Yang, B. Yin, Y. Sun, H. Pan, W. Sun et al., Zinc anode for mild aqueous zinc-ion batteries: Challenges, strategies, and perspectives. Nano-Micro Lett. **14**, 42 (2022). https://doi.org/10.1007/s40820-021-00782-5
18. C. Yan, Y. Wang, X. Deng, Y. Xu, Cooperative chloride hydrogel electrolytes enabling ultralow-temperature aqueous zinc ion batteries by the hofmeister effect. Nano-Micro Lett. **14**, 98 (2022). https://doi.org/10.1007/s40820-022-00836-2
19. H. Jin, S. Dai, K. Xie, Y. Luo, K. Liu et al., Regulating interfacial desolvation and deposition kinetics enables durable Zn anodes with ultrahigh utilization of 80%. Small **18**(4), e2106441 (2022). https://doi.org/10.1002/smll.202106441
20. X. Lu, C. Zhao, A. Chen, Z. Guo, N. Liu et al., Reducing Zn-ion concentration gradient by SO_4^{2-}-immobilized interface coating for dendrite-free Zn anode. Chem. Eng. J. **451**, 138772 (2023). https://doi.org/10.1016/j.cej.2022.138772
21. K. Wu, J. Yi, X. Liu, Y. Sun, J. Cui et al., Regulating Zn deposition via an artificial solid-electrolyte interface with aligned dipoles for long life Zn anode. Nano-Micro Lett. **13**, 79 (2021). https://doi.org/10.1007/s40820-021-00599-2
22. M. Fayette, H.J. Chang, X. Li, D. Reed, High-performance InZn alloy anodes toward practical aqueous zinc batteries. ACS Energy Lett. **7**(6), 1888–1895 (2022). https://doi.org/10.1021/acsenergylett.2c00843
23. Y. Zhang, X. Yang, Y. Hu, K. Hu, X. Lin et al., Highly strengthened and toughened Zn-Li-Mn alloys as long-cycling life and dendrite-free Zn anode for aqueous zinc-ion batteries. Small **18**(17), e2200787 (2022). https://doi.org/10.1002/smll.202200787
24. H. Meng, Q. Ran, T.-Y. Dai, H. Shi, S.-P. Zeng et al., Surface-alloyed nanoporous zinc as reversible and stable anodes for high-performance aqueous zinc-ion battery. Nano-Micro Lett. **14**, 128 (2022). https://doi.org/10.1007/s40820-022-00867-9
25. C. Han, W. Li, H.K. Liu, S. Dou, J. Wang, Principals and strategies for constructing a highly reversible zinc metal anode in aqueous batteries. Nano Energy **74**, 104880 (2020). https://doi.org/10.1016/j.nanoen.2020.104880
26. Z. Zhu, H. Jin, K. Xie, S. Dai, Y. Luo et al., Molecular-level Zn-ion transfer pump specifically functioning on (002) facets enables durable Zn anodes. Small **18**(49), e2204713 (2022). https://doi.org/10.1002/smll.202204713
27. Z. Hu, F. Zhang, A. Zhou, X. Hu, Q. Yan et al., Highly reversible Zn metal anodes enabled by increased nucleation overpotential. Nano-Micro Lett. **15**, 171 (2023). https://doi.org/10.1007/s40820-023-01136-z
28. X. Song, L. Bai, C. Wang, D. Wang, K. Xu et al., Synergistic cooperation of Zn(002) texture and amorphous zinc phosphate for dendrite-free Zn anodes. ACS Nano **17**(15), 15113–15124 (2023). https://doi.org/10.1021/acsnano.3c04343
29. Y. Hao, D. Feng, L. Hou, T. Li, Y. Jiao et al., Gel electrolyte constructing Zn (002) deposition crystal plane toward highly stable Zn anode. Adv. Sci. **9**(7), e2104832 (2022). https://doi.org/10.1002/advs.202104832
30. M. Zhou, S. Guo, J. Li, X. Luo, Z. Liu et al., Surface-preferred crystal plane for a stable and reversible zinc anode. Adv. Mater. **33**(21), e2100187 (2021). https://doi.org/10.1002/adma.202100187
31. S. Hu, W.-X. Li, Sabatier principle of metal-support interaction for design of ultrastable metal nanocatalysts. Science **374**(6573), 1360–1365 (2021). https://doi.org/10.1126/science.abi9828
32. Z.W. Seh, J. Kibsgaard, C.F. Dickens, I. Chorkendorff, J.K. Nørskov et al., Combining theory and experiment in electrocatalysis: Insights into materials design. Science **355**(6312), eaad4998 (2017). https://doi.org/10.1126/science.aad4998
33. R. Parsons, The rate of electrolytic hydrogen evolution and the heat of adsorption of hydrogen. Trans. Faraday Soc. **54**, 1053–1063 (1958). https://doi.org/10.1039/TF9585401053
34. J.K. Nørskov, T. Bligaard, A. Logadottir, J.R. Kitchin, J.G. Chen et al., Trends in the exchange current for hydrogen evolution. J. Electrochem. Soc. **152**, J23 (2005). https://doi.org/10.1149/1.1856988
35. R. Kronberg, K. Laasonen, Reconciling the experimental and computational hydrogen evolution activities of Pt(111) through DFT-based constrained MD simulations. ACS Catal. **11**(13), 8062–8078 (2021). https://doi.org/10.1021/acscatal.1c00538
36. L. Kristinsdóttir, E. Skúlason, A systematic DFT study of hydrogen diffusion on transition metal surfaces. Surf. Sci. **606**(17–18), 1400–1404 (2012). https://doi.org/10.1016/j.susc.2012.04.028
37. J. Hafner, *Ab-initio* simulations of materials using VASP: Density-functional theory and beyond. J. Comput. Chem. **29**(13), 2044–2078 (2008). https://doi.org/10.1002/jcc.21057

38. J.P. Perdew, K. Burke, M. Ernzerhof, Generalized gradient approximation made simple. Phys. Rev. Lett. **77**, 3865–3868 (1996). https://doi.org/10.1103/PhysRevLett.77.3865
39. X.-G. Xiong, T. Yanai, Projector augmented wave method incorporated into gauss-type atomic orbital based density functional theory. J. Chem. Theory Comput. **13**(7), 3236–3249 (2017). https://doi.org/10.1021/acs.jctc.7b00404
40. G. Henkelman, B.P. Uberuaga, H. Jónsson, A climbing image nudged elastic band method for finding saddle points and minimum energy paths. J. Chem. Phys. **113**(22), 9901–9904 (2000). https://doi.org/10.1063/1.1329672
41. G. Henkelman, H. Jónsson, A dimer method for finding saddle points on high dimensional potential surfaces using only first derivatives. J. Chem. Phys. **111**(15), 7010–7022 (1999). https://doi.org/10.1063/1.480097
42. F. Calle-Vallejo, J.I. Martínez, J.M. García-Lastra, P. Sautet, D. Loffreda, Fast prediction of adsorption properties for platinum nanocatalysts with generalized coordination numbers. Angew. Chem. Int. Ed. **53**(32), 8316–8319 (2014). https://doi.org/10.1002/anie.201402958
43. R. Tran, Z. Xu, B. Radhakrishnan, D. Winston, W. Sun et al., Surface energies of elemental crystals. Sci. Data **3**, 160080 (2016). https://doi.org/10.1038/sdata.2016.80
44. A. Aramata, S. Taguchi, T. Fukuda, M. Nakamura, G. Horányi, Underpotential deposition of zinc ions at single crystal electrodes and the effect of the adsorbed anions. Electrochim. Acta **44**, 999–1007 (1998). https://doi.org/10.1016/S0013-4686(98)00204-7
45. P. Lindgren, G. Kastlunger, A.A. Peterson, A challenge to the $G \sim 0$ interpretation of hydrogen evolution. ACS Catal. **10**(1), 121–128 (2020). https://doi.org/10.1021/acscatal.9b02799
46. G. Feng, F. Ning, J. Song, H. Shang, K. Zhang et al., Sub-2 nm ultrasmall high-entropy alloy nanoparticles for extremely superior electrocatalytic hydrogen evolution. J. Am. Chem. Soc. **143**(41), 17117–17127 (2021). https://doi.org/10.1021/jacs.1c07643
47. E. Skúlason, V. Tripkovic, M.E. Björketun, S. Gudmundsdóttir, G. Karlberg et al., Modeling the electrochemical hydrogen oxidation and evolution reactions on the basis of density functional theory calculations. J. Phys. Chem. C **114**(42), 18182–18197 (2010). https://doi.org/10.1021/jp1048887
48. H. Cao, Q. Wang, Z. Zhang, H.M. Yan, H. Zhao et al., Engineering single-atom electrocatalysts for enhancing kinetics of acidic Volmer reaction. J. Am. Chem. Soc. **145**(24), 13038–13047 (2023). https://doi.org/10.1021/jacs.2c13418
49. R. Kronberg, H. Lappalainen, K. Laasonen, Revisiting the Volmer-Heyrovský mechanism of hydrogen evolution on a nitrogen doped carbon nanotube: constrained molecular dynamics *versus* the nudged elastic band method. Phys. Chem. Chem. Phys. **22**(19), 10536–10549 (2020). https://doi.org/10.1039/C9CP06474E
50. Y. Tian, J. Hong, D. Cao, S. You, Y. Song et al., Visualizing Eigen/Zundel cations and their interconversion in monolayer water on metal surfaces. Science **377**(6603), 315–319 (2022). https://doi.org/10.1126/science.abo0823
51. D. Yuan, J. Zhao, H. Ren, Y. Chen, R. Chua et al., Anion texturing towards dendrite-free Zn anode for aqueous rechargeable batteries. Angew. Chem. Int. Ed. **60**(13), 7213–7219 (2021). https://doi.org/10.1002/anie.202015488
52. J. Zhang, W. Huang, L. Li, C. Chang, K. Yang et al., Non-epitaxial electrodeposition of (002)-textured Zn anode on textureless substrates for dendrite-free and hydrogen evolution-suppressed Zn batteries. Adv. Mater. **35**(21), e2300073 (2023). https://doi.org/10.1002/adma.202300073
53. X. Zhang, J. Li, D. Liu, M. Liu, T. Zhou et al., Ultra-long-life and highly reversible Zn metal anodes enabled by a desolvation and deanionization interface layer. Energy Environ. Sci. **14**(5), 3120–3129 (2021). https://doi.org/10.1039/D0EE03898A

 https://doi.org/10.1007/s40820-024-01337-0